



Peroxymonosulfate enhanced photodegradation of sulfamethoxazole with $\text{TiO}_2@\text{CuCo}_2\text{O}_4$ catalysts under simulated solar light

Oumaima Mertah^b, Almudena Gómez-Avilés^a, Abdelhak Kherbeche^{b,*}, Carolina Belver^a, Jorge Bedia^{a,*}

^a Chemical Engineering Department, Universidad Autónoma de Madrid, Campus Cantoblanco, E-28049 Madrid, Spain

^b Laboratory of Materials, Processes, Catalysis, and Environment (LPCME), Sidi Mohamed Ben Abdellah University, Fez, Morocco

ARTICLE INFO

Editor: Xin Yang

Keywords:

TiO_2
 CuCo_2O_4
 Photocatalysis
 Peroxymonosulfate
 Sulfamethoxazole
 Water treatment

ABSTRACT

Solar-light-assisted photocatalytic activation of peroxymonosulfate (PMS) is an effective advanced oxidation method for degrading pollutants in water. In this study, several TiO_2 supported on CuCo_2O_4 photocatalysts were successfully synthesized through simple hydrothermal and calcination method with different ratios of TiO_2 . The synthesized materials were tested for photocatalytic degradation of sulfamethoxazole (SMX) enhanced by PMS activation. The $\text{TiO}_2@\text{CuCo}_2\text{O}_4$ heterostructures showed a significantly higher photocatalytic degradation of SMX comparing with that of pure CuCo_2O_4 . The $\text{TiO}_2@\text{CuCo}_2\text{O}_4$ heterostructure with 20% of TiO_2 (TO-20-CCO) achieved the highest SMX removal, due to the synergistic effect between CuCo_2O_4 and TiO_2 . Besides, the reaction mechanisms induced by $\text{TiO}_2@\text{CuCo}_2\text{O}_4/\text{PMS}$ system were examined using trapping tests, which showed that sulfate ($\text{SO}_4^{\cdot-}$), hydroxyl (HO^{\cdot}) and superoxide ($\text{O}_2^{\cdot-}$) radicals were the most involved in the degradation reaction. The photodegradation mechanism seems to be based in the formation of a n-n heterojunction. This work details an efficient strategy for the synthesis of heterostructured photocatalysts using PMS as activator to degrade the antibiotic residues present in wastewater using solar light irradiation.

1. Introduction

Environmental pollution arising from antibiotics residues is receiving a great deal of attention in recent years. Many antibiotics, such as sulfamethoxazole, tetracycline, ciprofloxacin, and trimethoprim, among others, have been founded in surface and ground waters at variable concentrations [1–3]. Some of them are toxic, non- or low biodegradable and consequently, persistent. It is thus required to develop new materials and technologies for the degradation of antibiotic residues in the aquatic environment. Sulfamethoxazole (SMX) is a common sulfonamide antibiotic drug used for the treatment of various human and veterinary infections, and as food additive to endorse growth and gains. Due to its widespread use, it has been detected in the outlet stream of water treatment plants (WWTPs) with the subsequent potential danger to ecosystems and human health [1,4,5]. SMX is recalcitrant to conventional processes of the WWTPs [6]. For this reason, the implementation of highly efficient and stable methods for the removal and degradation of this and other antibiotics is mandatory. Among the different treatment options, solar photocatalysis can be considered a

suitable, cost-effective, and eco-friendly approach to achieve the SMX degradation. However, this technology has still a large margin for development, especially regarding the degradation of recalcitrant antibiotic contaminants, due to the limited activity of the photocatalysts.

One of the alternatives to enhance the solar photodegradation of refractory pollutants is the combination of the photocatalyst with different oxidant agents, such as hydrogen peroxide, ozone, persulfate, and/or peroxymonosulfate (PMS) [7,8]. Peroxymonosulfate-based advanced oxidation processes (PMS-AOPs) have been considered as an efficient method based on the suitable characteristics of PMS, namely chemical stability, relatively low cost, and suitable transport and storage [9]. PMS possesses a long O–O bond (1.326 Å) and asymmetric structure that demands less energy to be broken. This may facilitate its activation, as well as improve its oxidation efficiency to generate sulfate ($\text{SO}_4^{\cdot-}$) and hydroxyl (HO^{\cdot}) free radicals [10] through ultrasound, irradiation, heat, electrochemistry, or the action of semiconductors, transition metals, or carbon-based catalysts [11–16]. These radicals possess high oxidation capacity ($\text{SO}_4^{\cdot-}$; $E^0 = 2.5 - 3.1 \text{ V}_{\text{NHE}}/\text{HO}^{\cdot}$; $E^0 = 1.8 - 2.8 \text{ V}_{\text{NHE}}$). Sulfate radicals are characterized by a longer half-life (30–40 μs) than hydroxyl

* Corresponding authors.

E-mail addresses: abdelhak.kherbeche@usmba.ac.ma (A. Kherbeche), jorge.bedia@uam.es (J. Bedia).

<https://doi.org/10.1016/j.jece.2022.108438>

Received 19 April 2022; Received in revised form 6 July 2022; Accepted 11 August 2022

Available online 19 August 2022

2213-3437/© 2022 The Author(s). Published by Elsevier Ltd. This is an open access article under the CC BY-NC-ND license (<http://creativecommons.org/licenses/by-nc-nd/4.0/>).

ones ($<1 \mu\text{s}$) and they have also probed good oxidation behavior of different antibiotics in a wide pH range of 2.0 – 8.0 [17].

Activation of PMS with transition metals (e.g., Co, Ni, Fe, Mn) have aroused great interest due to low energy demands, and economical and easy handling operation. Co(II) ions are considered a very effective homogeneous activator of PMS [18]. However, its application suffered from certain shortcomings due to the difficult recovery of the ions, which lead to the creation of secondary pollution. To overcome this problem, cobalt-based heterogeneous photocatalysts have been reported to be efficient and stable for PMS activation. In particular, Cu-Co bimetallic photocatalysts have been synthesized to enhance the water stability. Copper cobaltite (CuCo_2O_4), as one of the bimetallic spinel oxide aroused as an interesting semiconductor with a narrow band gap (1.6–1.8 eV) and a promising potential for energy, photoelectrical, and catalytic applications. The simultaneous participations of both redox couples $\text{Co}^{3+}/\text{Co}^{2+}$ and $\text{Cu}^{2+}/\text{Cu}^{3+}$ enhanced the redox reactions in comparison with the single metallic oxide, which can improve the photocatalytic activity. Meanwhile, the high conductivity of CuCo_2O_4 , due to the relatively low activation energy of electron transfer between the cations, enhances the electron transfer rate and the charge separation efficiency [19,20]. After years of extensive research, various modification strategies have been developed to improve the photocatalytic activity of promising CuCo_2O_4 , including doping or combination with other materials (e.g., $\text{V}_2\text{O}_5/\text{CuCo}_2\text{O}_4$ [19], $\text{X-CuCo}_2\text{O}_4$ (X = Cr, Fe, Mo)/ CuCo_2O_4 [21,22], $\text{ZnO}/\text{CuCo}_2\text{O}_4$ [23], $\text{CuCo}_2\text{S}_4/\text{CuCo}_2\text{O}_4$ [24], $\text{g-C}_3\text{N}_4/\text{CuCo}_2\text{O}_4$ [25] etc.). To date, titanium dioxide (TiO_2) still emerged as an attractive candidate for heterogeneous photocatalysis because of exceptional stability, non-toxicity, biologically inertness and high reactivity [26–28]. However, the application of TiO_2 based photocatalysts is hampered due to its ineffectual use of solar energy and low charge separation [29]. Despite these inherent drawbacks, the semiconductor combination is the main factor to avoid the above limitation for practical application. Very few studies have analyzed the photoactivity of transition metal spinels combined with TiO_2 . Coromelci et al. [30] studied the photodegradation of a dye with $\text{TiO}_2/\text{ZnFe}_2\text{O}_4$ heterostructures prepared by ultrasound template-assisted sol-gel method. Ahmadpour et al. [31] concluded that $\text{TiO}_2@\text{ZnFe}_2\text{O}_4/\text{Pd}$ nanocomposite significantly improved the photodegradation of diclofenac under direct solar irradiation. Magdalane et al. [32] prepared TiO_2 doped CoFe_2O_4 nanostructures to improve the photocatalytic degradation of Congo Red dye under visible light. Xu et al. [33] prepared $\text{CuCo}_2\text{O}_4/\text{TiO}_2$ for H_2 production and demonstrated that the efficient separation of charge carriers due to the p-n junction adopting the interfacial Ti-O-Cu/Co bonds is crucial for the improved performance and photostability. These modifications may effectively decrease the band gap energy and expand light absorption range of TiO_2 , as well as alter the band structure and improve the separation of charge carriers [33].

In this research, a simple hydrothermal-calcination method was used to synthesize CuCo_2O_4 spinels with incorporated TiO_2 particles at different mass ratios. The purpose of this work is to demonstrate the outstanding effect of the coexistence of CuCo_2O_4 and TiO_2 particles and explore the pathways for the activation of PMS to degrade SMX. The antibiotic degradation was found to increase with increasing TiO_2 loading in the composite, achieving a total degradation of SMX after 180 min under simulated solar light irradiation. This is the first study analyzing the photocatalytic behavior of $\text{CuCo}_2\text{O}_4/\text{TiO}_2$ heterostructures with peroxymonosulfate.

2. Experimental section

2.1. Materials

Copper (II) nitrate trihydrate ($\text{Cu}(\text{NO}_3)_2 \cdot 3\text{H}_2\text{O}$), cobalt(II) nitrate hexahydrate ($\text{Co}(\text{NO}_3)_2 \cdot 6\text{H}_2\text{O}$), sodium hydroxide (NaOH), TiO_2 (P25), sulfamethoxazole (SMX, $\text{C}_{10}\text{H}_{11}\text{N}_3\text{O}_3\text{S}$), peroxymonosulfate (PMS,

OXONE®, $\text{KHSO}_5 \cdot 0.5\text{KHSO}_4 \cdot 0.5\text{K}_2\text{SO}_4$), phenol (Ph, $\geq 96\%$), *tert*-butyl alcohol (TBA, $\geq 99\%$), *p*-benzoquinone (p-BQ, $\geq 98\%$), sodium chlorite (NaCl), sodium bicarbonate (NaHCO_3) and sodium hydroxide (NaOH, pellets) were obtained from Sigma-Aldrich. Acetonitrile (ACN, UV HPLC grade), acetic acid ($\geq 99\%$), absolute ethanol (EtOH, 99.7%), sodium sulfate (Na_2SO_4) and hydrochloric acid (HCl, 37%) were acquired from Scharlab. Sodium nitrate (NaNO_3), potassium bicarbonate (KHCO_3), and humic acid (HA) were obtained from Panreac, while potassium iodide (KI) was supplied by Fluka. All the chemicals were used as received without further purification. Ultrapure deionized water ($18.2 \text{ M}\Omega\cdot\text{cm}$) was used in all the study, except for the solutions of SMX that were performed with deionized water (type II).

2.2. Synthesis of $\text{TiO}_2\text{-CuCo}_2\text{O}_4$

$\text{TiO}_2@\text{CuCo}_2\text{O}_4$ heterostructures were synthesized by hydrothermal synthesis [34]. Firstly, 0.2 mmol of $\text{Cu}(\text{NO}_3)_2 \cdot 0.3 \text{H}_2\text{O}$ and 0.4 mmol of $\text{Co}(\text{NO}_3)_2 \cdot 0.6 \text{H}_2\text{O}$ were dissolved in an ethanol and water solution (1:4 vol.) under continuous stirring. Later, the corresponding amount of TiO_2 (20, 40 or 60 wt% of the theoretical CuCo_2O_4) was added until obtaining a homogeneous solution. Then, NaOH solution (3 M) was added dropwise into the above mixture to adjust the pH to 8–9. The mixture was maintained under stirring for one hour and then, it was sealed into a 100 mL Teflon-lined autoclave and heated at 180°C for 8 h. After natural cooling, the obtained black precipitate was collected by centrifugation, washed four times with ethanol and ultrapure water and dried overnight at 60°C . Finally, the solid was annealed at 400°C (heating rate of $3^\circ\text{C}\cdot\text{min}^{-1}$) for 4 h under air atmosphere in a muffle furnace. The synthesized photocatalysts were labeled as TO-X-CCO, where X represents the TiO_2 weight ratio of (20, 40 or 60%). For comparison, pristine CuCo_2O_4 was prepared using the same process without the addition of TiO_2 .

2.3. Characterization

The crystal structure of the samples was identified using an X-ray diffractometer (XRD, Bruker D8 Discover) equipped with $\text{Cu K}\alpha$ radiation source ($\lambda = 0.154 \text{ nm}$) in a 2θ scanning range from 10° to 70° . The morphologies were characterized using a scanning electron microscope (SEM, HITACHI S-4800) provided with X-ray energy dispersive spectroscopy (EDS) for measuring the microanalysis of the material, previously conformed as a pellet. N_2 adsorption-desorption at -196°C was performed using a TriStar 123 equipment (Micromeritics II 3020). The total surface area, S_{BET} , was calculated by the Brunauer-Emmett-Teller (BET) method [35], and the microporous volume (V_{MP}) and external surface area (S_{EXT}) were quantified by the *t*-plot [36]. Microporous surface area (S_{MP}) was calculated as the difference between S_{BET} and S_{EXT} . The total pore volume was estimated using the amount of nitrogen adsorbed at a relative pressure (P/P_0) of 0.99. Previously, the samples were outgassed under vacuum before analyzing at 120°C overnight (VacPrep 60, Micromeritics). UV-vis diffuse reflectance spectra were collected using a UV-Vis spectrophotometer (DRS, Shimadzu UV2600) in the wavelength range from 200 to 800 nm using BaSO_4 as reference material. The band gap (E_g) values were determined from the UV-vis DRS spectra by the Tauc Plot method [37], considering the photocatalysts as indirect semiconductors. Settling tests were performed as a quantification of the separation of the photocatalysts from the treated streams using an UV-vis spectrophotometer (Shimadzu UV2600) [38]. To determine the settled catalyst, the time evolution of the absorbance at 600 nm of catalyst suspensions ($1 \text{ g}\cdot\text{L}^{-1}$) was measured continuously in a quartz cuvette for 4 h. PMS concentration was followed using an Agilent Technologies UV-vis spectrophotometer (Cary 60). A Metrohm Autolab potentiostat equipment (PGSTAT204) was used to determine the electrochemical properties of the different materials. This system comprises an indium tin oxide (DropSens ITO10) working electrode, with counter and reference counterparts of carbon and silver electrodes, respectively

[39,40]. The materials suspensions ($1 \text{ mg} \cdot \text{mL}^{-1}$) were prepared in $0.1 \text{ M Na}_2\text{SO}_4$ ($\text{pH} \sim 4.5$ at 25°C) and placed into the electrochemical cell. Electrochemical impedance spectroscopy (EIS) was registered scanning the frequency range from 10^5 to 10^{-1} Hz at a fixed potential of -1.2 V , whereas Mott-Schottky (M-S) plots were obtained applying a voltage between -1.5 and 0.4 V under a constant frequency of 100 Hz . The flat band potential of the material, V_{fb} , was obtained following Mott-Schottky equation (Eq. 1) [41]:

$$\frac{1}{C^2} = \frac{2}{\varepsilon \cdot \varepsilon_0 \cdot e \cdot N_D} \left(V - V_{\text{fb}} - \frac{k \cdot T}{e} \right), \quad (1)$$

being C the capacitance of the semiconductor-electrolyte junction at applied voltage V ; ε and ε_0 the permittivity of the semiconductor and the void, respectively; e the electron charge; k the Boltzmann's constant; and T the temperature. V_{fb} is estimated from the intercept point of the tangent line with the potential axis in the plot of $1/C^2$ vs V . The potential of the conduction band (V_{CB}) can be calculated with respect to the normal hydrogen electrode (NHE) at $\text{pH} 7$ following a Nernstian shift using Eq. 2 [42].

$$V_{\text{CB}} = V_{\text{fb(Ag/AgCl,pH)}} + \Delta V_{\text{(Ag/AgCl,NHE)}} - 0.059(7 - \text{pH}), \quad (2)$$

where $\Delta V_{\text{(Ag/AgCl, NHE)}}$ is the Ag/AgCl potential against NHE (0.21 V). Finally, the valence band potential (V_{VB}) can be estimated following Eq. 3:

$$V_{\text{VB}} = V_{\text{CB}} + E_g/e, \quad (3)$$

where E_g is the bandgap of the semiconductor.

2.4. Photocatalytic degradation experiments

The photocatalytic activities of the different materials were tested in the degradation of SMX solutions (initial concentration, $5 \text{ mg} \cdot \text{L}^{-1}$) under solar radiation in a Suntest XLS+ simulator (ATLAS®) equipped with a Xenon lamp emitting $600 \text{ W} \cdot \text{m}^{-2}$ and a light correction filter $\lambda \leq 290 \text{ nm}$. Typically, in a Pyrex jacketed closed reactor, $250 \text{ mg} \cdot \text{L}^{-1}$ of as-prepared photocatalyst was dispersed into 150 mL SMX solution at natural pH under stirring and at controlled temperature (25°C). The dispersion was initially maintained in dark for 60 min to achieve the adsorption equilibrium. Afterwards, 2.283 mg of PMS were added to the solution, resulting in a PMS concentration of 0.05 mM , and the lamp was turned on. At different irradiation times, aliquots of $450 \mu\text{L}$ were extracted from the reaction medium and filtered using Whatman $0.2 \mu\text{m}$ PTFE syringeless filters (Scharlab) to separate the photocatalyst.

The concentration of the SMX was analyzed using a High-Performance liquid chromatograph (HPLC; Shimadzu Prominence-I LC-2030 C) equipped with a Diode Array detector (SPD-M30A) and a C-18 column (Eclipse Plus $5 \mu\text{m}$, Agilent) by an isocratic $70/30\%$ method of a mixture of 0.1% v/v acetic acid and acetonitrile as mobile phase with a flow rate of $0.8 \text{ mL} \cdot \text{min}^{-1}$ at 35°C . The absorption wavelength for SMX detection was set at 268 nm . Blank tests were carried out without catalyst at the same reaction conditions to check the stability of the SMX pollutant under solar simulated irradiation, showing negligible photocatalytic degradation. All degradation experiments were performed in triplicate and average values were represented. Error bars indicate the standard deviation based on these triplicate measurements.

Quenching experiments were carried out with phenol (Ph), ethanol (EtOH), *tert*-butyl alcohol (TBA) and *p*-benzoquinone (*p*-BQ). Phenol (0.3 mM) was used to trap sulfate and hydroxyl radicals formed on the solid-interface because of its weak polarity, relative easiness to approach catalyst surface and its high rate constants of the reactions with both radicals [40]. Similarly, ethanol (3.3 mM) can also react with hydroxyl and sulfate radicals through its alpha hydrogen. *Tert*-butyl alcohol (3.3 mM) with no alpha hydrogen is used as an effective scavenger for hydroxyl radicals (HO^\bullet) [43], while *p*-benzoquinone (3.3 mM) is used as

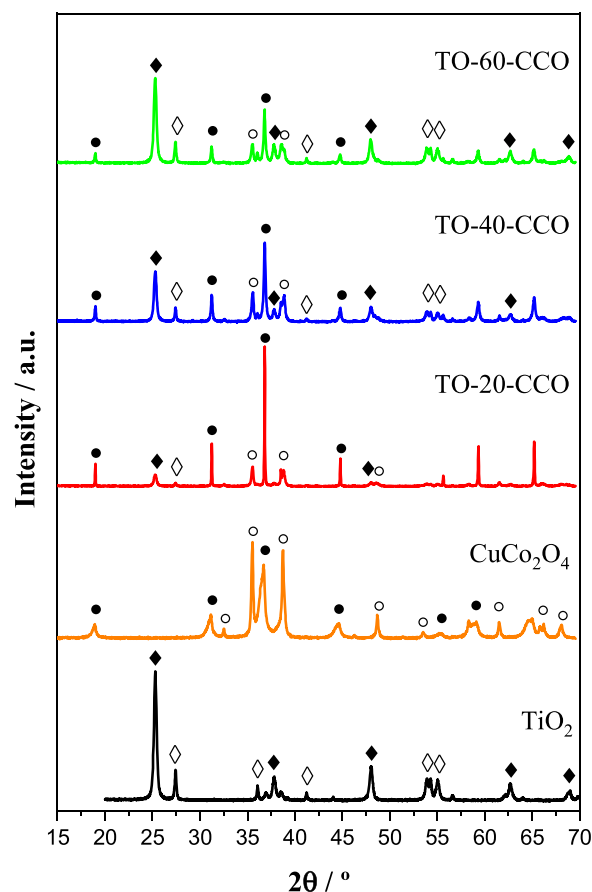


Fig. 1. XRD patterns. \blacklozenge Anatase tetragonal (JCPDS 78–2486; JCPDS 21–1272); \diamond Rutile tetragonal (JCPDS 21–1276); \bullet CuCo_2O_4 (JCPDS 37–0878); \circ CuO (JCPDS 45–0937).

superoxide radicals ($\text{O}_2^{\bullet-}$) scavenger. These experiments were performed under the same reaction conditions described above just adding the scavenger to the SMX solution after the dark adsorption equilibrium step. The influence of some inorganic ions frequently present in water was also explored. The tests were carried out in the presence of Cl^- ($25 \text{ mg} \cdot \text{L}^{-1}$), NO_3^- ($50 \text{ mg} \cdot \text{L}^{-1}$) and SO_4^{2-} ($50 \text{ mg} \cdot \text{L}^{-1}$), and HCO_3^- ($150 \text{ mg} \cdot \text{L}^{-1}$) [44]. On the other hand, the influence of the presence of organic matter was analyzed including humic acid (HA) ($20 \text{ mg} \cdot \text{L}^{-1}$). To quantify the PMS concentration, a solution of potassium iodide (KI, $40.0 \text{ g} \cdot \text{L}^{-1}$) and potassium bicarbonate (KHCO_3 , $5.0 \text{ g} \cdot \text{L}^{-1}$) was used [45]. This solution (5.0 mL) was mixed with 0.1 mL of filtered sample and left 20 min for reaction. Then, the chromogenic sample was analyzed by UV spectrophotometer at $\lambda = 352 \text{ nm}$.

3. Results and discussion

3.1. Characterization

The crystalline structures of TiO_2 , CuCo_2O_4 and all TO-X-CCO heterostructures were studied by X-ray diffraction (XRD). Fig. 1 represents the XRD patterns of all samples. The pattern of CuCo_2O_4 shows diffraction peaks at 18.9 , 31.1 , 36.7 , 44.6 , 55.5 , 59.2 and 65.1° that agree with the spinel (face-centered cubic structure) oxide of this material (JCPDS file no. 37–0878) and can be assigned to (111), (220), (311), (400), (422), (333) and (440) crystal planes, respectively. This pattern has also less intense diffraction peaks at 32.5 , 35.5 , 38.7 , 48.7 , 53.1 , 62.0 , 65.8 and 68.1° characteristic of the (110), (002), (-202), (020), (-113), (-311) and (220) reflections of monoclinic CuO (JCPDS file no. 37–0878), suggesting the formation of a low amount of CuO

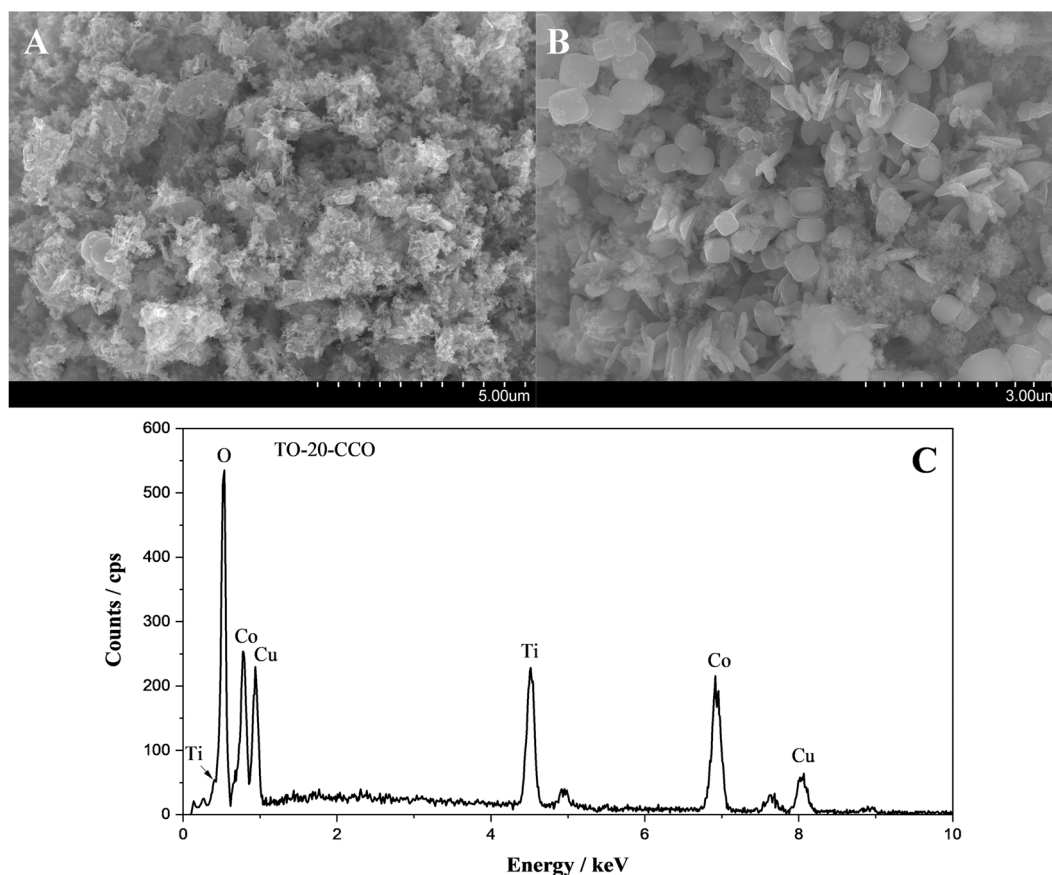


Fig. 2. SEM images of A) spinel (CuCo_2O_4) and B) TO-20-CCO; C) EDX pattern for TO-20-CCO.

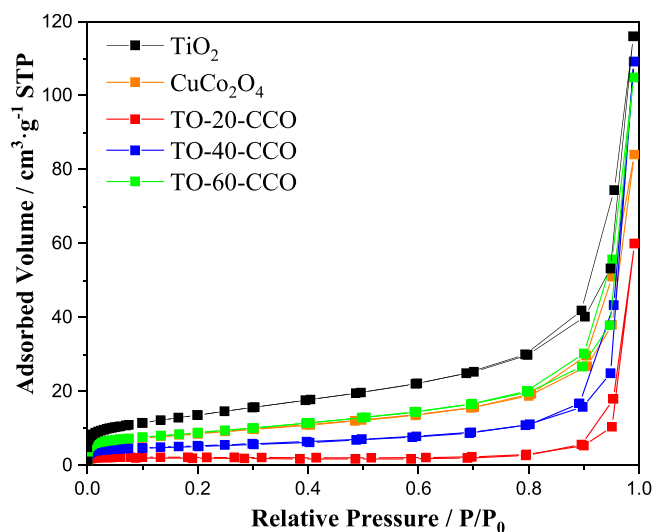


Fig. 3. N_2 adsorption-desorption isotherms at -196°C .

during the synthesis. No other phases are observed, discarding the formation of other copper or cobalt oxides. The XRD pattern of TiO_2 shows the diffraction peaks of tetragonal anatase and rutile phases characteristic of P25 precursor. The anatase phase (JCPDS file no. 21-1272) [33] has diffraction peaks at 25.6° , 38.3° , 48.4° , 63.0° and 69.3° ascribed to (101), (004), (200), (204) and (116) reflections, respectively. The tetragonal rutile phase (JCPDS file no. 21-1276) is characterized by the diffraction peaks observed at 27.7° , 36.2° , 41.6° , 54.6° and 56.6° typical of the reflections of the crystal planes (110), (101), (111), (211) and (220),

respectively. All diffractograms of TO-X-CCO heterostructures show the coexistence of both CuCo_2O_4 and TiO_2 , with variable amounts depending on their formulation. Thus, the diffraction peaks of anatase and rutile are more intense with increasing TiO_2 content, with decreasing proportion of CuO .

Fig. 2 A and B show SEM micrographs of CuCo_2O_4 and TO-20-CCO, respectively. CuCo_2O_4 image (Fig. 2A) is a representative low-magnification SEM image of this sample with many sheets aggregated to each other [33,46]. When TiO_2 was anchored on CuCo_2O_4 , this is partially covered with TiO_2 particles with disk-like morphology (Fig. 2B), which seems to support the successful formation of the heterostructure in TO-20-CCO. Fig. 2C depicts the energy dispersive spectrum (EDS) of TO-20-CCO. It confirms the presence of dispersive peaks corresponding to O, Ti, Cu and Co elements. The atomic ratio of Co:Cu is approximately 2:1 (estimated from EDS analysis), which is consistent with the stoichiometric ratio of CuCo_2O_4 .

Fig. 3 represents the nitrogen adsorption-desorption isotherms at -196°C of CuCo_2O_4 and the different TiO_2 - CuCo_2O_4 heterostructures. All the isotherms are similar and can be classified as type-IV based on the International Union of Pure and Applied Chemistry (IUPAC) classification, with H3-type hysteresis loops, characteristic of the presence of slit-shape mesoporosity [47]. It seems that the presence of TiO_2 in the synthesis process can affect the porosity of the formed CuCo_2O_4 . The lowest amount of TiO_2 analyzed (20% on TO-20-CCO) results in a significant decrease of the amount of N_2 adsorbed at low relative pressures, suggesting a lower formation of micropores in the structure of CuCo_2O_4 in the presence of TiO_2 . The increase of the TiO_2 content results in an increase of the amount of N_2 adsorbed, probably as a consequence of the more developed porosity of TiO_2 . Table 1 details the characteristic parameters of porous textures of the different materials, which confirmed the discussed above in the basis of the nitrogen isotherms. All the

Table 1
Crystallite size, porous texture parameters and band gap values (Eg).

Samples	S_{BET}^a ($\text{m}^2\cdot\text{g}^{-1}$)	S_{MP}^b ($\text{m}^2\cdot\text{g}^{-1}$)	S_{EXT}^c ($\text{m}^2\cdot\text{g}^{-1}$)	V_{total}^d ($\text{cm}^3\cdot\text{g}^{-1}$)	V_{MP}^e ($\text{cm}^3\cdot\text{g}^{-1}$)	Band Gap (eV)
TiO ₂	49	2	47	0.179	0.001	3.3
CuCo ₂ O ₄	30	3	27	0.130	0.002	1.6
TO-20-CCO	7	2	5	0.093	0.002	3.5
TO-40-CCO	18	5	13	0.169	0.003	3.5
TO-60-CCO	31	2	29	0.162	0.001	3.5

^a Specific surface area; ^b Microporous surface area; ^c External surface area; ^d Total pore volume; ^e Micropore volume.

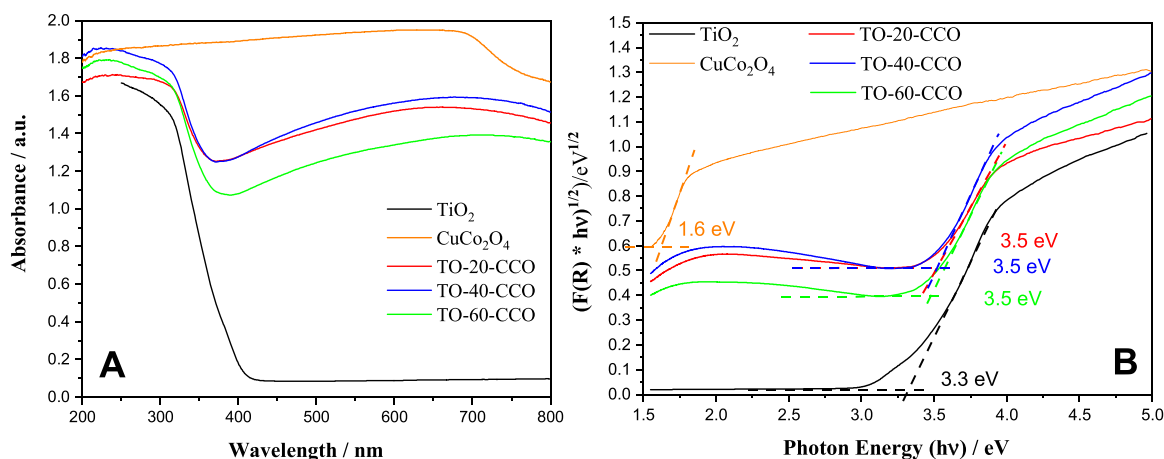


Fig. 4. UV-visible diffuse absorbance spectra (A) and Tauc plots (B).

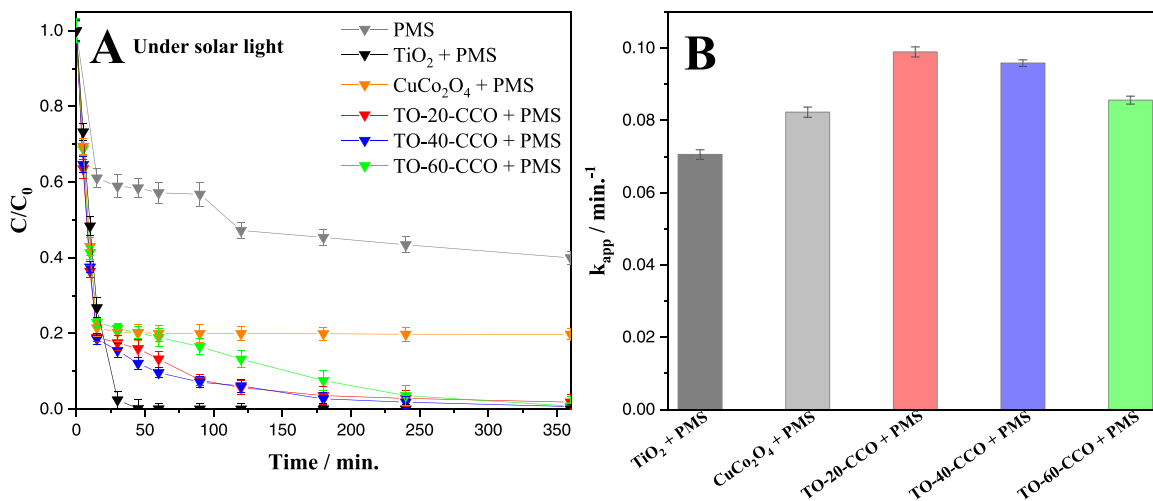


Fig. 5. (A) Time-course evolution of SMX with PMS under simulated solar light (Photocatalyst dosage: 250 $\text{mg}\cdot\text{L}^{-1}$; [SMX]₀: 5 $\text{mg}\cdot\text{L}^{-1}$; [PMS]: 0.05 mM; Intensity: 600 $\text{W}\cdot\text{m}^{-2}$); (B) Apparent first order rate constants.

samples show relatively low surface area values ($< 50 \text{ m}^2\cdot\text{g}^{-1}$), with negligible contribution of microporosity, as confirm the very low V_{MP} values [25].

Fig. 4 A depicts the UV-VIS DRS spectra of CuCo₂O₄, TiO₂ and TO-X-CCO heterostructures. CuCo₂O₄ shows a red shifted absorption edge in the range between 650 and 800 nm, due to its narrow bandgap and black color. All TO-X-CCO heterostructures show a clear absorption edge at wavelengths below 400 nm (UV range) attributed to the band-to-band transition of TiO₂ [48]. But they also absorb a significant amount of radiation in the visible range (between 400 and 800 nm), due to the presence of CuCo₂O₄, which confers to the heterostructures their characteristic black color. This effect is more evident in TO-20-CCO and TO-40-CCO, because these materials have higher proportions of

CuCo₂O₄. The formation of a heterostructure between CuCo₂O₄ and TiO₂ is expected to ameliorate the light absorption ability in terms of photoactivation role of CuCo₂O₄ that is responsible of electron transfer from CuCo₂O₄ to TiO₂. Besides, the direct bandgaps of samples were calculated according to the Tauc plots [49], as shown in Fig. 4B, considering the heterostructures as indirect semiconductors (like the bare TiO₂). The values are slightly higher than that of pure TiO₂ (3.3 eV), indicating that the interaction with spinel does not modify significantly the TiO₂ band gap in any case.

3.2. SMX degradation tests

The TO-X-CCO heterostructures were tested for the SMX degradation

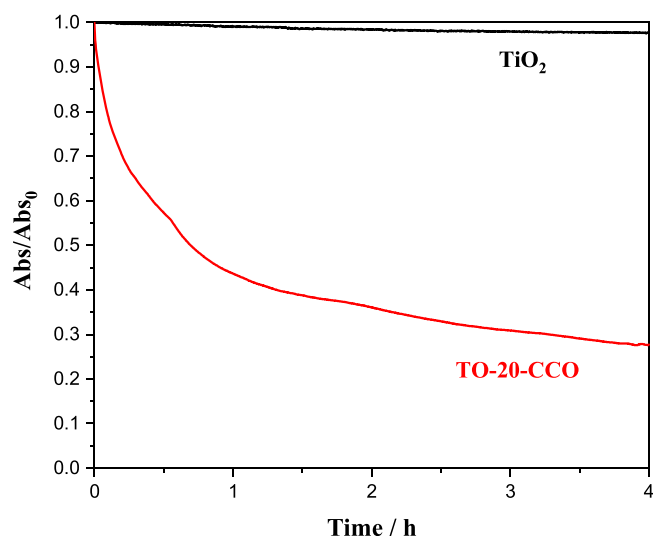


Fig. 6. Absorbance evolution profiles (600 nm) during settling test of TO-20-CCO and TiO₂ suspensions (1 g·L⁻¹).

with PMS under simulated solar light, after observing that SMX adsorption before adding PMS was negligible in all cases. Fig. 5A represents the SMX evolution with irradiation time in the presence of PMS. CuCo₂O₄ exhibited a very fast initial degradation of SMX that, regrettably, stops after the first reaction minutes. After 6 h of irradiation, about 80% of SMX degradation is observed. Photolysis/PMS system can degrade SMX, reaching 60% of pollutant removal after 6 h. It seems that a high number of radicals (HO[•] and SO₄^{•-}) are generated from PMS under

light irradiation [50] at the beginning of the reaction, as indicates the very fast SMX removal in the first reaction minutes. However, it is most likely that this high number of radicals results also in a fast recombination into non-active species, which justifies the low activity observed for the rest of the reaction. The best results were obtained with the TiO₂@CuCo₂O₄ heterostructures that accelerated the SMX degradation and achieved complete SMX degradation after 6 h. This may be attributed to the prompt redox cycle of Co²⁺/Co³⁺ in TiO₂@CuCo₂O₄ system that allows the activation of PMS to produce HO[•] and SO₄^{•-} to oxidize SMX under simulated sunlight [51]. Fig. 5B summarizes the values of the apparent pseudo-first-order rate constants obtained with the different samples. TiO₂@CuCo₂O₄ heterostructures show slightly higher values than bare TiO₂ and CuCo₂O₄, although TiO₂ overpass the SMX degradation of the rest of the samples after the first 15 min of reaction. The highest kinetic rate was achieved using TO-20-CCO ($k = 0.10 \text{ min}^{-1}$) in the range of the values reported for the SMX degradation in other studies. In this sense, Berruti and co-workers [52] degraded SMX (100 µg·L⁻¹) with an apparent rate constant of 0.05 min⁻¹ with PMS (0.01 mM) under natural solar light. Yang et al. degraded 52% of SMX under visible light with a rate constant of 0.055 min⁻¹ using TiO_{2-x}/rGO and persulfate [53]. Yan et al. [54] achieved 99% of SMX degradation over CuO@Al₂O₃ (EPC)/PMS in 120 min with an initial SMX solution of 10 mg·L⁻¹, catalyst charge of 0.5 g·L⁻¹, PMS concentration of 60.9 mg·L⁻¹ and initial solution pH of 6.2 in the absence of light. In the same way, Zhu et al. [55] synthesized a novel magnetic MnFe₂O₄/GCNS nanosheet nanocomposite that achieves a complete removal of SMX (5 mg·L⁻¹) with PMS (45.7 mg·L⁻¹) with a reaction rate constant of 0.1363 min⁻¹ in 35 min. In another study [56], the concentration of SMX (6.3 mg·L⁻¹) was reduced by approximate 88.5% within 6 min in the MoS₂/Fe²⁺/PMS process where the concentration of

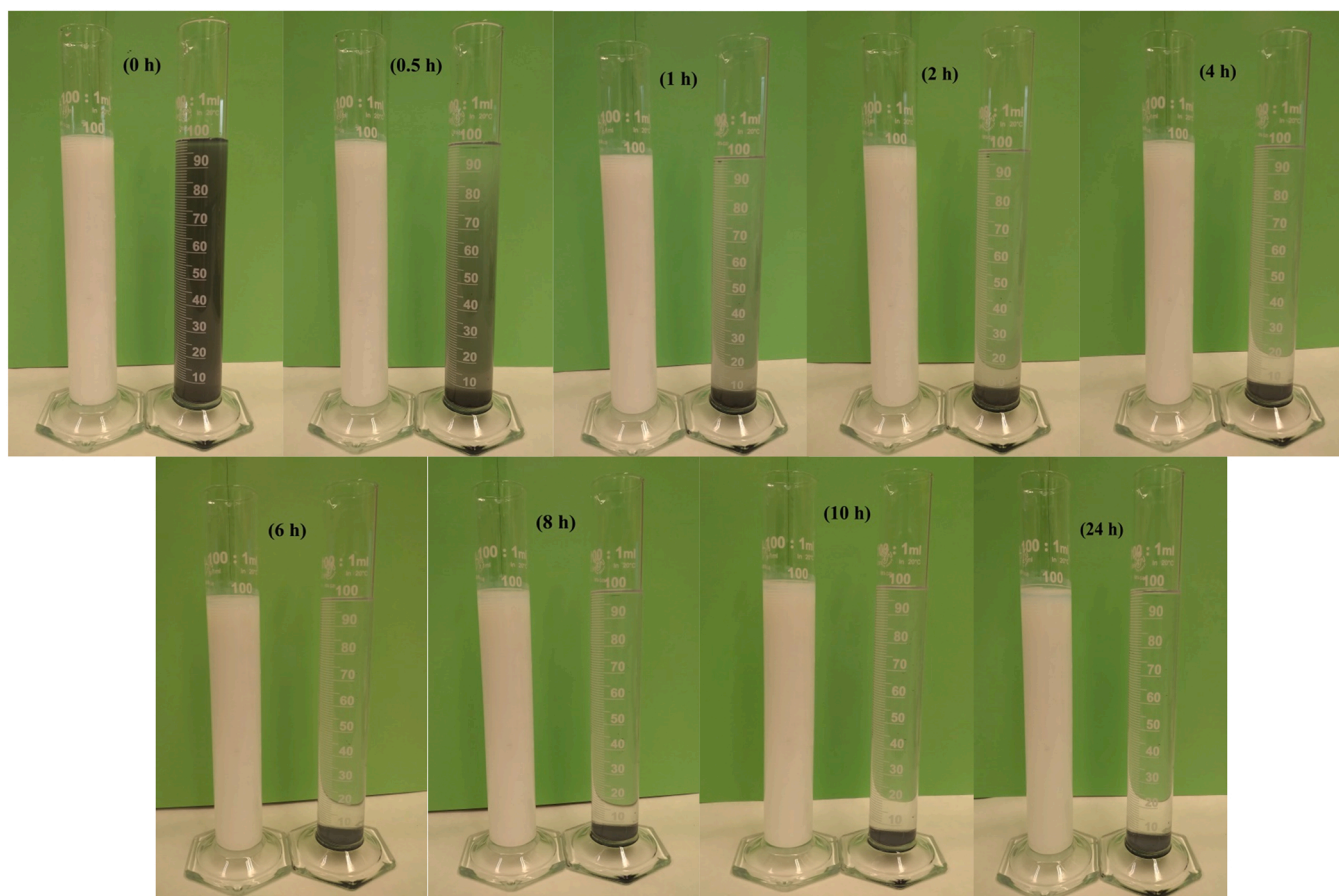


Fig. 7. Settling test in test tubes for TiO₂ (left) and TO-20-CCO (right) suspensions (1 g·L⁻¹).

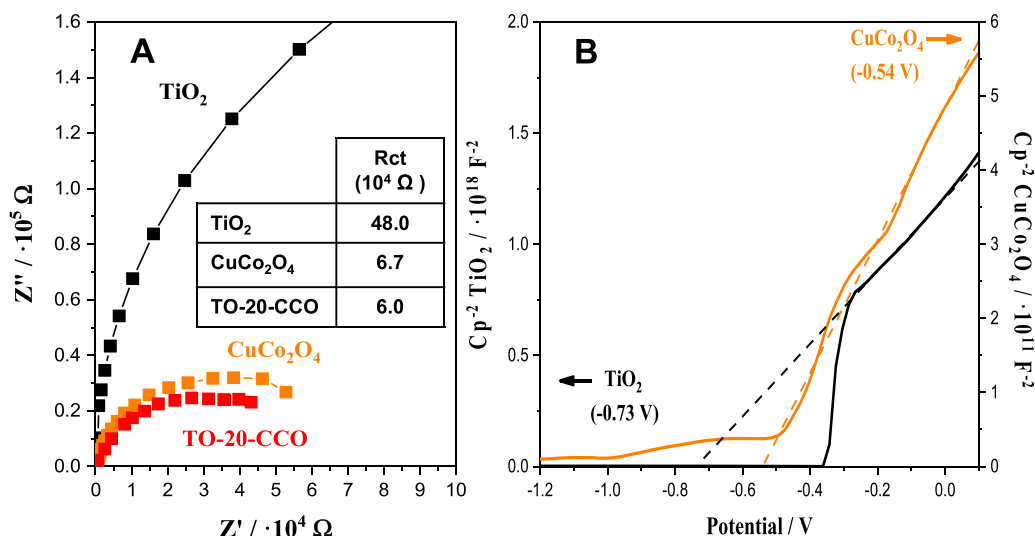


Fig. 8. (A) EIS Nyquist plots of TiO₂, CuCo₂O₄ and TO-20-CCO and charge transfer resistance (R_{ct}) values, and (B) Mott-Schottky plots of TiO₂ and CuCo₂O₄.

MoS₂ was 0.3 g·L⁻¹, Fe²⁺ 70 μM, and PMS, 46.1 mg·L⁻¹, and initial pH 3.0. This improvement was due to the incorporation of Fe²⁺ in the media because if they only used the MoS₂/PMS system, SMX was degraded around 20% within 6 min. With our TO-20-CCO/PMS system was possible to degrade 37% of SMX (5 mg·L⁻¹) within 5 min with a lower amount of PMS (15.2 mg·L⁻¹).

Consequently, the heterostructures synthesized in this study show great potential for PMS activation. Although, it is also true that their activity is similar to that of the TiO₂. However, it should be considered that photoactivity is not the only characteristic that influences the interest of a photocatalyst. The separation of the spent photocatalyst from the water after use is a crucial aspect for the implementation in real applications. In this sense, to evaluate the recovery potential of the heterostructures from the reaction mixture after reaction, settling tests with TiO₂ and TO-20-CCO suspensions were performed in quartz cuvette inside a UV-Vis spectrometer. Fig. 6 shows the evolution of absorbance of the suspensions (1 g·L⁻¹) with the settling time. It is very clear the much better behavior observed with TO-20-CCO, which shows a much higher settling rate than TiO₂. After 4 h, almost all TO-20-CCO particles are deposited in the bottom of the quartz cuvette, while TiO₂ particles remained unsettled. This may be attributed to the aggregation of the particles as observed in SEM micrographs that makes them settle very fast [38]. This makes the synthesized heterostructures very interesting for real applications, since they show a high activity in the SMX degradation, but also an easier separation from the aqueous media after use. This is confirmed by Fig. 7 that shows pictures of the evolution with time of the settling process of TiO₂ and TO-20-CCO suspensions (1 g·L⁻¹). It is very clear the much higher settling velocity of TO-20-CCO heterostructure than of TiO₂. The heterostructure seems almost completely settled after only 1 h. In contrast, TiO₂ suspension remains unsettled even after 24 h. This means a clear advantage of the TO-20-CCO synthesized in this study in relation with TiO₂.

Electrochemical characterization was also assessed to rationalize the causes of the better photocatalytic activity of TO-20-CCO. In this sense, the charge transfer resistance has been analyzed by EIS through the Nyquist plots [57,58], which are represented in Fig. 8A. TO-20-CCO shows the smallest arc radius, which means that it has the lowest charge transfer resistance (R_{ct} values in inset table in Fig. 8A), which indicates a more efficient use of the separated charges due to the lower interfacial charge transfer resistance, and consequently a better charge mobility [59]. This results in more photo-induced carriers that can participate in redox reactions per unit time, thereby enhancing photocatalytic activity. Besides, Fig. 8B display the Mott-Schottky plots of TiO₂ and CuCo₂O₄. The positive slopes of the plots confirms that both

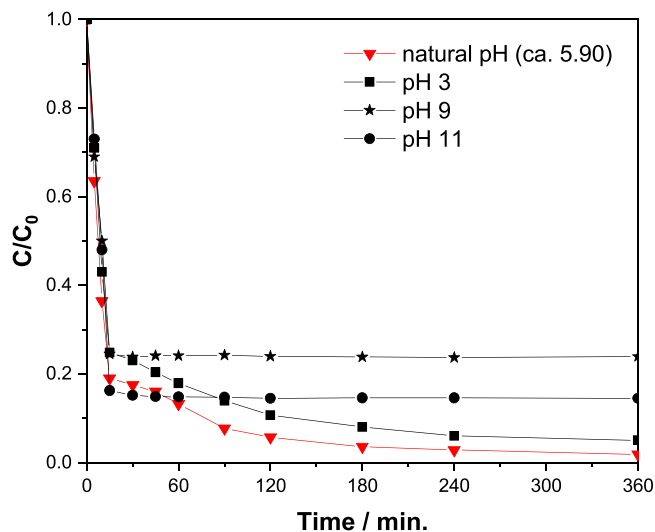


Fig. 9. SMX photodegradation at different initial pH in the TO-20-CCO/PMS system under solar irradiation (operating conditions as in Fig. 5).

materials act as n-type semiconductors. From the intercepts of the extrapolated lines, the flat band potentials (V_{fb}) of TiO₂ and CuCo₂O₄ can be estimated in -0.73 and -0.54 V, respectively. Using Eq. 2, the positions of the conduction bands, V_{CB} , of each material were determined to be at -0.53 and -0.34 V, respectively. Finally, Eq. 3 allows to obtain the valence band positions, V_{VB} , considering the bandgap values, E_g , of each material (Table 1).

Fig. 9 shows the effect of different initial solution pH (3.0, 9.0 and 11) on the photodegradation of SMX. The conversions of SMX after 360 min of reaction were 96, 99, 76 and 85 at initial pH values of 3, natural (ca. 5.9), 9.0, and 11.0, respectively. It has been previously reported that PMS showed the poorest stability at pH values close to 9, when HSO₅⁻ decomposes to SO₅²⁻ [60], in agreement with the lowest conversion SMX conversion obtained at this pH. Moreover, it should be mentioned that the solution pH had an important effect on SMX speciation. SMX has three different species (i.e., cationic, neutral and anionic) at different pH values due to its two pK_a values (1.6 and 5.7). At pH of 3 and 5, the SMX molecules are mostly neutral, which can justify the better reactivity at these pH values. In contrast, at pH values higher than 7 the SMX molecules are mainly negatively charged, which seems to

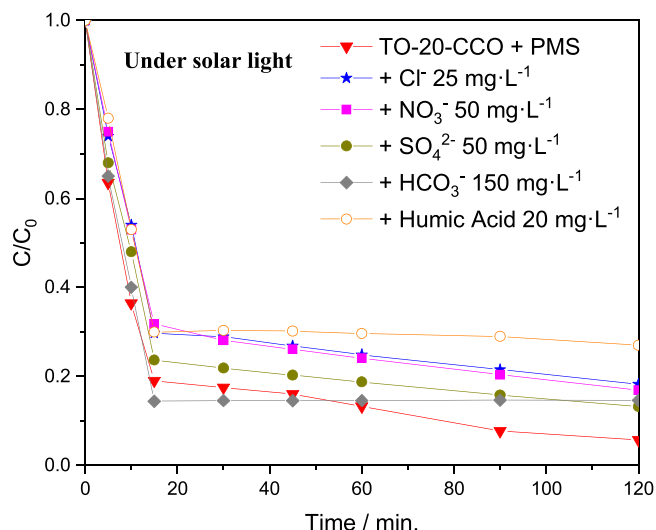


Fig. 10. Effect of some inorganic ions and humic acid on the degradation of SMX with TO-20-CCO/PMS system under solar irradiation (operating conditions as in Fig. 5).

have lower reactivity [54] supporting the obtained data.

It is well-known that the presence of ions in the water can alter the degradation of pollutants [61]. Therefore, the effect of different ions, such as Cl^- , NO_3^- , SO_4^{2-} , and HCO_3^- on the degradation of SMX in the TO-20-CCO/PMS system was analyzed (Fig. 10). The presence of any of the ions had slight negative effects on the degradation of SMX. In the case of Cl^- , it could be oxidized by highly active free radicals ($SO_4^{\bullet-}$ and HO^{\bullet}) into less active free radicals (Cl^{\bullet} and $HOCl^{\bullet-}$), preventing the degradation of SMX [54,62]. In the case of NO_3^- , it can react with $SO_4^{\bullet-}$ to generate NO_3^{\bullet} radical, which is also less reactive. Bicarbonate ions resulted in a very slight improvement of the initial degradation of SMX. This radical might act as a promoter stimulating PMS decomposition into HO^{\bullet} or $SO_4^{\bullet-}$ [63]. The effect of the presence of organic matter was analyzed by using humic acid. As shown in Fig. 10, the SMX degradation at the end of the reaction was significantly reduced. $SO_4^{\bullet-}$ and HO^{\bullet} radicals could react with HA at high rates, supporting the observed inhibitory effect of HA due to the quenching of $SO_4^{\bullet-}$ and HO^{\bullet} [56].

Quenching experiments were performed with different scavengers to analyze the role of the different reactive oxygen species (ROS) in the SMX degradation in the TO-20-CCO/PMS system under simulated solar light. Fig. 11A represents the time-course evolution of SMX

concentration with different scavengers (Ph, EtOH, TBA and *p*-BQ), while Fig. 11B displays the apparent first-order reaction kinetic constants of those tests. The degradation of SMX was drastically reduced in the presence of Ph ($k = 0.019 \text{ min}^{-1}$), which indicates the determinant role of both HO^{\bullet} and $SO_4^{\bullet-}$ radicals formed on the TO-20-CCO/PMS solid-interface system. When *p*-BQ was added to the reaction system, the degradation efficiency of SMX also dropped significantly ($k = 0.033 \text{ min}^{-1}$). Thus, it was assumed that superoxide radicals, $O_2^{\bullet-}$, also contributed to the degradation of SMX. Conversely, EtOH and TBA had a lower effect on the degradation of SMX ($k = 0.060$ and 0.065 min^{-1} , respectively), which indicated the minor contribution of HO^{\bullet} and $SO_4^{\bullet-}$ radicals in the solution [64,65].

Fig. 12 represents the evolution of PMS concentration in the absence and presence of the different scavengers during the SMX degradation with TO-20-CCO/PMS under solar irradiation. The high PMS decomposition efficiency is evidenced by this system. As can be seen, the presence of EtOH produced a very slight inhibition effect on PMS decomposition. However, in the presence of TBA, and to a greater extent with *p*-BQ, a significant reduction of the PMS decomposition is observed. This can be due to the higher hydrophobicity of TBA and *p*-BQ

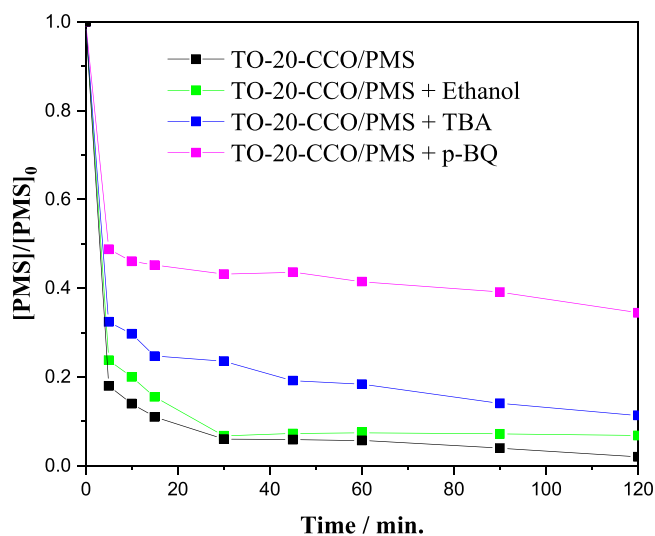


Fig. 12. Evolution of PMS concentration in the absence and presence of the different scavengers during the SMX degradation with TO-20-CCO/PMS system under solar irradiation (operating conditions as in Fig. 5).

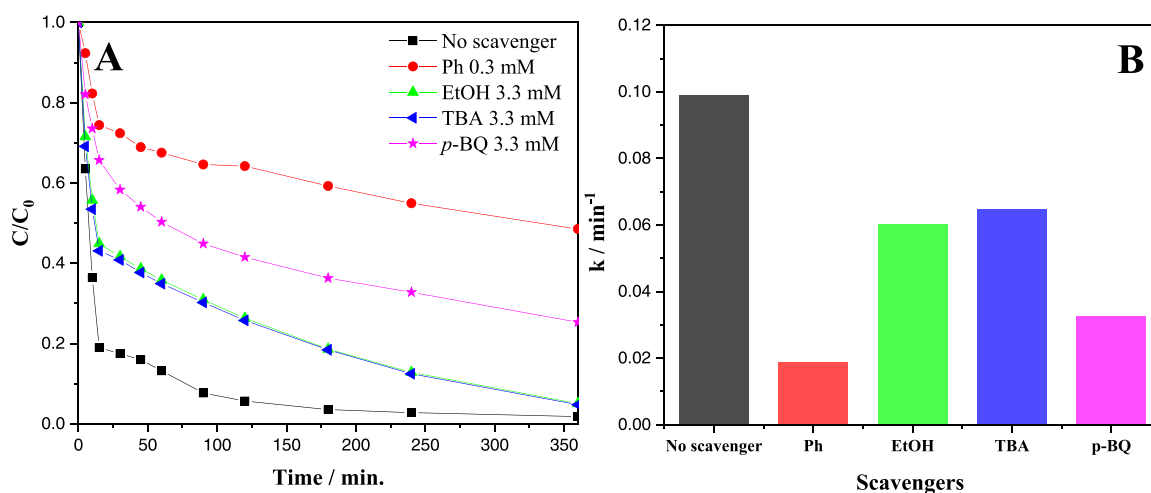


Fig. 11. (A) Effect of radical scavengers on SMX degradation using TO-20-CCO/PMS, and (B) values of the pseudo-first order rate constant of SMX disappearance (k_{app}). (Photocatalyst dosage: 250 $mg \cdot L^{-1}$; $[SMX]_0$: 5 $mg \cdot L^{-1}$; $[PMS]$: 0.05 mM; Intensity: 600 $W \cdot m^{-2}$).

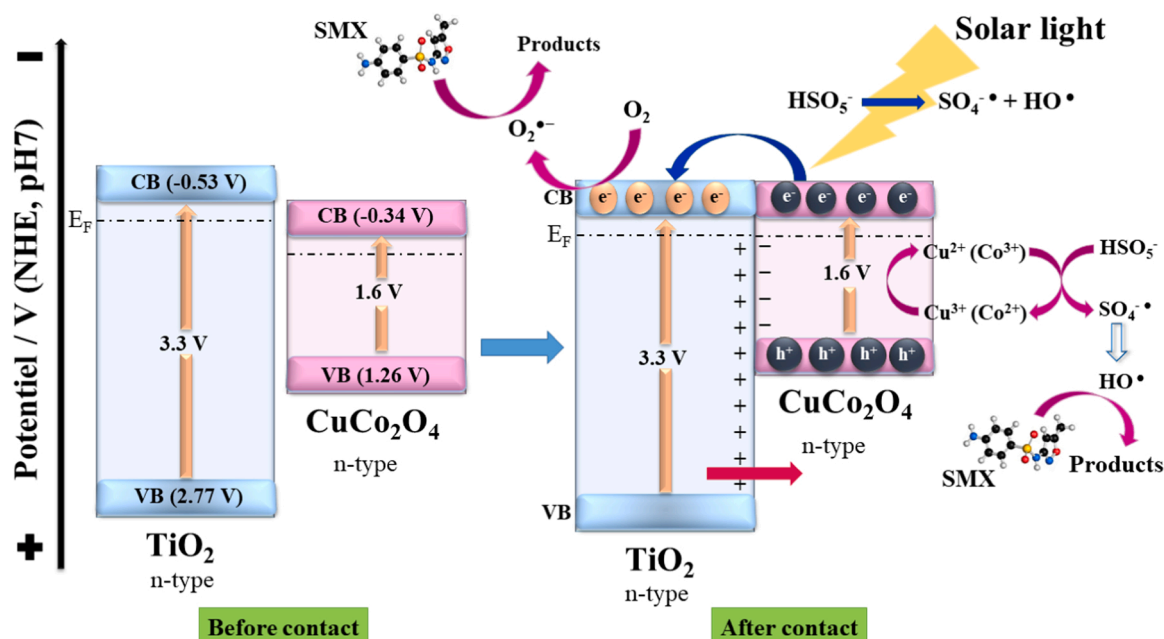
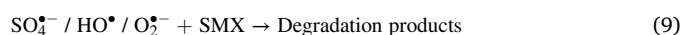
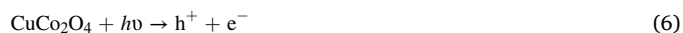
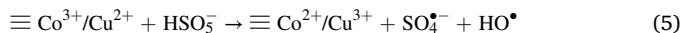


Fig. 13. Proposed photocatalytic mechanism of SMX.

than EtOH, so probably they cover active sites for PMS adsorption and/or activation processes and are likely to quench aqueous radicals rather than surface-bound ones [45,66]. In the case of phenol scavenger, UV-visible spectroscopy quantification was not possible to measure due to absorption interference."

Considering the above results and the band edge positions of TiO₂ and CuCo₂O₄ previously calculated, a schematic degradation diagram related to the formation of n-n heterojunction between TiO₂ and CuCo₂O₄ is proposed in Fig. 13. It is shown the energy of the band gap, the edges of the valence and conduction bands of both TiO₂ and CuCo₂O₄ before contact. Due to n-type characteristics of TiO₂ and CuCo₂O₄ semiconductors, their Fermi levels (E_F) are located close to the conduction band (CB) [67]. Furthermore, the Fermi level of TiO₂ is more negative than that of CuCo₂O₄. Consequently, after contact of these semiconductors and form an n-n heterojunction, electrons migrate from TiO₂ to CuCo₂O₄ until their Fermi levels equalize. This results in a depletion layer (positive region) on TiO₂ side and an accumulation layer (negatively charged region) on CuCo₂O₄ side. When the process reaches an equilibrium state (equalized Fermi level), a built-in electric field is established in the junction area with the field direction from TiO₂ to CuCo₂O₄ (red arrow in Fig. 13) [68]. On the other hand, band gap of CuCo₂O₄ is narrower than that of TiO₂. Thus, under simulated solar light, electron-hole pairs are preferably produced in CuCo₂O₄ rather than in TiO₂. The built-in field promotes the separation of photo-generated carriers in CuCo₂O₄ and facilitates the electrons flowing towards the CB of TiO₂, meanwhile the photogenerated holes are effectively collected in the VB of CuCo₂O₄. In such a way, the photo-generated charge carriers are effectively separated, electron-hole recombination is reduced, which can result in the observed enhanced photoactivity under solar irradiation. Based in the band alignment and taking into account the role of the different species suggested by the quenching tests, a reaction mechanism for the SMX degradation in TiO₂/CuCo₂O₄-PMS system is proposed (Fig. 13). PMS in the water solution can decompose homogeneously under irradiation into $SO_4^{\bullet-}$ and HO^{\bullet} radicals (Eq. 4) [69,70]. PMS activation reaction also happens by a single electron transfer process in the presence of metal oxide couple, Cu (II) and Co(III) sites (Eq. 5) [71]. Simultaneously, solar light was absorbed by CuCo₂O₄ which is able to generate charge pairs (e^-/h^+) (Eq. 6). The excited electrons are transformed to the TiO₂ conduction band where they react with dissolved O₂ to generate $O_2^{\bullet-}$ radicals (Eq.

7), which according to the quenching tests are involved in the reaction [50,51]. Electron transfer between the metal pairs through redox reaction (Eq. 8) could regenerate the metal reaction sites of the spinel. Finally, the different generated radicals could oxidize SMX into the reaction byproducts (Eq. 9).



4. Conclusions

TiO₂-CuCo₂O₄ heterostructures were synthesized through simple hydrothermal and calcination method with different ratios of TiO₂. The synthesized materials have been tested in the solar photocatalytic degradation of SMX enhanced by PMS activation. The method achieves excellent interface contact and strong interaction between CuCo₂O₄ and TiO₂, thus promoting absorption of visible light and enhancing separation and migration of photogenerated electron-hole pairs. Specifically, the heterostructures show the lowest charge transfer resistance, and consequently the best charge mobility. This results in more photo-induced carriers that can participate in redox reactions per unit time, thereby enhancing photocatalytic activity. We proposed the formation of a n-n heterojunction, being HO^{\bullet} , $SO_4^{\bullet-}$ and $O_2^{\bullet-}$ the main reactive species involved in the PMS assisted SMX degradation. The results of this study confirm the promising behavior of the TiO₂/CuCo₂O₄/PMS system in the SMX degradation.

CRediT authorship contribution statement

Conceptualization, A.K., C.B. and J.B.; methodology, A.G.-A. and O. M.; writing - original draft, A.G.-A. and O.M; writing - review & editing,

A.K., C.B. and J.B.; supervision, A.K., C.B. and J.B.; funding acquisition, C.B. and J.B. All authors have read and agreed to the published version of the manuscript.

Declaration of Competing Interest

The authors declare that they have no known competing financial interests or personal relationships that could have appeared to influence the work reported in this paper.

Data availability

Data will be made available on request.

Acknowledgements

This research was funded by the Spanish State Research Agency (PID2019-106186RB-I00/AEI/10.13039/501100011033, Spain).

References

- [1] M.H. de Matos Rodrigues, P.A. Rodrigues de Sousa, K.C.M. Borges, L. de Melo Coelho, R. de Fátima Gonçalves, M.D. Teodoro, F. Vilella da Motta, R. Maribondo do Nascimento, M.G. Júnior, Enhanced degradation of the antibiotic sulfamethoxazole by heterogeneous photocatalysis using $\text{CeO}_2/\text{g-C}_3\text{N}_4$ particles, *J. Alloy. Compd.* 808 (2019), 151711, <https://doi.org/10.1016/J.JALLCOM.2019.151711>.
- [2] Y. Bao, T.T. Lim, R. Goei, Z. Zhong, R. Wang, X. Hu, One-step construction of heterostructured metal-organics/ Bi_2O_3 with improved photoinduced charge transfer and enhanced activity in photocatalytic degradation of sulfamethoxazole under solar light irradiation, *Chemosphere* 205 (2018) 396–403, <https://doi.org/10.1016/J.CHEMOSPHERE.2018.04.031>.
- [3] Q. Cai, J. Hu, Effect of UVA/LED/ TiO_2 photocatalysis treated sulfamethoxazole and trimethoprim containing wastewater on antibiotic resistance development in sequencing batch reactors, *Water Res.* 140 (2018) 251–260, <https://doi.org/10.1016/J.WATRES.2018.04.053>.
- [4] A. Mirzaei, L. Yerushalmi, Z. Chen, F. Haghighat, J. Guo, Enhanced photocatalytic degradation of sulfamethoxazole by zinc oxide photocatalyst in the presence of fluoride ions: Optimization of parameters and toxicological evaluation, *Water Res.* 132 (2018) 241–251, <https://doi.org/10.1016/J.WATRES.2018.01.016>.
- [5] H. Gong, W. Chu, Permanganate with a double-edge role in photodegradation of sulfamethoxazole: Kinetic, reaction mechanism and toxicity, *Chemosphere* 191 (2018) 494–502, <https://doi.org/10.1016/J.CHEMOSPHERE.2017.10.086>.
- [6] R. Wei, F. Ge, S. Huang, M. Chen, R. Wang, Occurrence of veterinary antibiotics in animal wastewater and surface water around farms in Jiangsu Province, China, *Chemosphere* 82 (2011) 1408–1414, <https://doi.org/10.1016/J.CHEMOSPHERE.2010.11.067>.
- [7] Y. Feng, C. Liao, L. Kong, D. Wu, Y. Liu, P.H. Lee, K. Shih, Facile synthesis of highly reactive and stable Fe-doped $\text{g-C}_3\text{N}_4$ composites for peroxymonosulfate activation: A novel nonradical oxidation process, *J. Hazard. Mater.* 354 (2018) 63–71, <https://doi.org/10.1016/J.JHAZMAT.2018.04.056>.
- [8] Z.H. Diao, J.C. Jin, M.Y. Zou, H. Liu, J.Q. Qin, X.H. Zhou, W. Qian, P.R. Guo, L. J. Kong, W. Chu, Simultaneous degradation of amoxicillin and norfloxacin by TiO_2/nZVI composites coupling with persulfate: Synergistic effect, products and mechanism, *Sep. Purif. Technol.* 278 (2021), 119620, <https://doi.org/10.1016/J.SEPPUR.2021.119620>.
- [9] D. Dai, Z. Yang, Y. Yao, L. Chen, G. Jia, L. Luo, Highly efficient removal of organic contaminants based on peroxymonosulfate activation by iron phthalocyanine: mechanism and the bicarbonate ion enhancement effect, *Catal. Sci. Technol.* 7 (2017) 934–942, <https://doi.org/10.1039/C6CY02317G>.
- [10] H. Wang, B. Liao, M. Hu, Y. Ai, L. Wen, S. Yang, Z. Ye, J. Qin, G. Liu, Heterogeneous activation of peroxymonosulfate by natural chalcophyllite for efficient remediation of groundwater polluted by aged landfill leachate, *Appl. Catal. B: Environ.* 300 (2022), 120744, <https://doi.org/10.1016/J.APCATB.2021.120744>.
- [11] J. Wang, H. B. M. Yang, R. Liu, C. Hu, H. Liu, J. Qu, Anaerobically-digested sludge disintegration by transition metal ions-activated peroxymonosulfate (PMS): Comparison between Co^{2+} , Cu^{2+} , Fe^{2+} and Mn^{2+} , *Sci. Total Environ.* 713 (2020), 136530 <https://doi.org/10.1016/J.SCTOTENV.2020.136530>.
- [12] M. Noorisepehr, K. Ghadirinejad, B. Kakavandi, A. Ramazanpour Esfahani, A. Asadi, Photo-assisted catalytic degradation of acetaminophen using peroxymonosulfate decomposed by magnetic carbon heterojunction catalyst, *Chemosphere* 232 (2019) 140–151, <https://doi.org/10.1016/J.CHEMOSPHERE.2019.05.070>.
- [13] B. Kakavandi, N. Bahari, R. Rezaei Kalantary, E. Dehghani Fard, Enhanced sono-photocatalysis of tetracycline antibiotic using TiO_2 decorated on magnetic activated carbon (MAC@T) coupled with US and UV: A new hybrid system, *Ultrason. Sonochem.* 55 (2019) 75–85, <https://doi.org/10.1016/J.ULTSONCH.2019.02.026>.
- [14] R. Khaghani, B. Kakavandi, K. Ghadirinejad, E. Dehghani Fard, A. Asadi, Preparation, characterization and catalytic potential of $\gamma\text{-Fe}_2\text{O}_3/\text{AC}$ mesoporous heterojunction for activation of peroxymonosulfate into degradation of cyfluthrin insecticide, *Microporous Mesoporous Mater.* 284 (2019) 111–121, <https://doi.org/10.1016/J.MICROMESO.2019.04.013>.
- [15] T. Zhang, H. Zhu, J.P. Croué, Production of sulfate radical from peroxymonosulfate induced by a magnetically separable CuFe_2O_4 spinel in water: Efficiency, stability, and mechanism, *Environ. Sci. Technol.* 47 (2013) 2784–2791, https://doi.org/10.1021/ES304721G/SUPPL_FILE/ES304721G_SI_001.PDF.
- [16] S. Su, W. Guo, C. Yi, Y. Leng, Z. Ma, Degradation of amoxicillin in aqueous solution using sulphate radicals under ultrasound irradiation, *Ultrason. Sonochem.* 19 (2012) 469–474, <https://doi.org/10.1016/J.ULTSONCH.2011.10.005>.
- [17] K.K. Kefeni, B.B. Mamba, T.A.M. Msagati, Application of spinel ferrite nanoparticles in water and wastewater treatment: A review, *Sep. Purif. Technol.* 188 (2017) 399–422, <https://doi.org/10.1016/J.SEPPUR.2017.07.015>.
- [18] G.P. Anipsitakis, D.D. Dionysiou, Degradation of Organic Contaminants in Water with Sulfate Radicals Generated by the Conjunction of Peroxymonosulfate with Cobalt, *Environ. Sci. Technol.* 37 (2003) 4790–4797, <https://doi.org/10.1021/ES0263792>.
- [19] F. Hasanvandian, A. Shokri, M. Moradi, B. Kakavandi, S. Rahman Setayesh, Encapsulation of spinel CuCo_2O_4 hollow sphere in V_2O_5 -decorated graphitic carbon nitride as high-efficiency double Z-type nanocomposite for levofloxacin photodegradation, *J. Hazard. Mater.* 423 (2022), 127090, <https://doi.org/10.1016/J.JHAZMAT.2021.127090>.
- [20] D. Cheng, T. Wang, G. Zhang, H. Wu, H. Mei, A novel nonenzymatic electrochemical sensor based on double-shelled CuCo_2O_4 hollow microspheres for glucose and H_2O_2 , *J. Alloy. Compd.* 819 (2020), 153014, <https://doi.org/10.1016/J.JALLCOM.2019.153014>.
- [21] Z.K. Heiba, N.M. Farag, A.M. El-naggar, J.R. Plaisier, A.M. Aldhafiri, M. B. Mohamed, Influence of Cr and Fe doping on the structure, magnetic and optical properties of nano CuCo_2O_4 , *Ceram. Int.* 47 (2021) 7888–7897, <https://doi.org/10.1016/J.CERAMINT.2020.11.135>.
- [22] Z.K. Heiba, N.M. Farag, A.M. El-Naggar, M. Abdellatif, A.M. Aldhafiri, M. B. Mohamed, Effect of Mo-doping on the structure, magnetic and optical characteristics of nano CuCo_2O_4 , *J. Mater. Res. Technol.* 10 (2021) 832–839, <https://doi.org/10.1016/J.JMRT.2020.12.056>.
- [23] M. Habibi, A. Habibi-Yangjeh, M. Sabri, H. Chand, V. Krishnan, C. Wang, Highly impressive activation of persulfate ions by novel $\text{ZnO}/\text{CuCo}_2\text{O}_4$ nanostructures for photocatalytic removal of tetracycline hydrochloride under visible light, *Environ. Technol. Innov.* 24 (2021), 102038, <https://doi.org/10.1016/J.ETI.2021.102038>.
- [24] X. Xu, Y. Liu, P. Dong, P.M. Ajayan, J. Shen, M. Ye, Mesoporous $\text{CuCo}_2\text{S}_4/\text{CuCo}_2\text{O}_4$ nanoflowers as advanced electrodes for asymmetric supercapacitors, *J. Power Sources* 400 (2018) 96–103, <https://doi.org/10.1016/J.JPOWSOUR.2018.08.012>.
- [25] S.M.N. Jeghan, J.Y. Do, M. Kang, Fabrication of flower-like copper cobaltite/graphitic-carbon nitride ($\text{CuCo}_2\text{O}_4/\text{g-C}_3\text{N}_4$) composite with superior photocatalytic activity, *J. Ind. Eng. Chem.* 57 (2018) 405–415, <https://doi.org/10.1016/J.JIEC.2017.08.049>.
- [26] A. Fujishima, X. Zhang, D.A. Tryk, TiO_2 photocatalysis and related surface phenomena, *Surf. Sci. Rep.* 63 (2008) 515–582, <https://doi.org/10.1016/J.SURFREP.2008.10.001>.
- [27] V. Etacheri, C. di Valentin, J. Schneider, D. Bahnemann, S.C. Pillai, Visible-light activation of TiO_2 photocatalysts: Advances in theory and experiments, *J. Photochem. Photobiol. C: Photochem. Rev.* 25 (2015) 1–29, <https://doi.org/10.1016/J.JPHOTOCHEMREV.2015.08.003>.
- [28] H. Dong, G. Zeng, L. Tang, C. Fan, C. Zhang, X. He, Y. He, An overview on limitations of TiO_2 -based particles for photocatalytic degradation of organic pollutants and the corresponding countermeasures, *Water Res.* 79 (2015) 128–146, <https://doi.org/10.1016/J.WATRES.2015.04.038>.
- [29] C. Qiang, N. Li, S. Zuo, Z. Guo, W. Zhan, Z. Li, J. Ma, Microwave-assisted synthesis of $\text{RuTe}_2/\text{black TiO}_2$ photocatalyst for enhanced diclofenac degradation: Performance, mechanistic investigation and intermediates analysis, *Sep. Purif. Technol.* 283 (2022), 120214, <https://doi.org/10.1016/J.SEPPUR.2021.120214>.
- [30] C. Coromelci, M. Neamtu, M. Ignat, P. Samoilă, M.F. Zaltariu, M. Palamaru, Ultrasound assisted synthesis of heterostructured $\text{TiO}_2/\text{ZnFe}_2\text{O}_4$ and $\text{TiO}_2/\text{ZnFe}_{1.98}\text{La}_{0.02}\text{O}_4$ systems as tunable photocatalysts for efficient organic pollutants removal, *Ceram. Int.* (2021), <https://doi.org/10.1016/J.CERAMINT.2021.11.019>.
- [31] N. Ahmadvour, M.H. Sayadi, S. Sobhani, M. Hajiani, Photocatalytic degradation of model pharmaceutical pollutant by novel magnetic $\text{TiO}_2/\text{ZnFe}_2\text{O}_4/\text{Pd}$ nanocomposite with enhanced photocatalytic activity and stability under solar light irradiation, *J. Environ. Manag.* 271 (2020), 110964, <https://doi.org/10.1016/J.JENVMAN.2020.110964>.
- [32] C.M. Magdalane, G.M.A. Priyadharsini, K. Kaviyarasu, A.I. Jothi, G.G. Simiyon, Synthesis and characterization of TiO_2 doped cobalt ferrite nanoparticles via microwave method: Investigation of photocatalytic performance of congo red degradation dye, *Surf. Interfaces* 25 (2021), 101296, <https://doi.org/10.1016/J.SURFIN.2021.101296>.
- [33] C. Xu, C. Jin, W. Chang, X. Hu, H. Deng, E. Liu, J. Fan, Interfacially bonded $\text{CuCo}_2\text{O}_4/\text{TiO}_2$ nanosheet heterostructures for boosting photocatalytic H_2 production, *Catal. Sci. Technol.* 9 (2019) 4990–5000, <https://doi.org/10.1039/C9CY01209E>.
- [34] R. BoopathiRaja, M. Parthibavarman, A. Nishara Begum, Hydrothermal induced novel CuCo_2O_4 electrode for high performance supercapacitor applications, *Vacuum* 165 (2019) 96–104, <https://doi.org/10.1016/J.VACUUM.2019.04.013>.
- [35] S. Brunauer, P.H. Emmett, E. Teller, Adsorption of Gases in Multimolecular Layers, *J. Am. Chem. Soc.* 60 (2002) 309–319, <https://doi.org/10.1021/JA01269A023>.

- [36] B.C. Lippens, J.H. de Boer, Studies on pore systems in catalysts: V. The t method, *J. Catal.* 4 (1965) 319–323, [https://doi.org/10.1016/0021-9517\(65\)90307-6](https://doi.org/10.1016/0021-9517(65)90307-6).
- [37] J. Tauc, Absorption edge and internal electric fields in amorphous semiconductors, *Mater. Res. Bull.* 5 (1970) 721–729, [https://doi.org/10.1016/0025-5408\(70\)90112-1](https://doi.org/10.1016/0025-5408(70)90112-1).
- [38] M. Peñas-Garzón, A. Gómez-Avilés, J. Bedia, J.J. Rodríguez, C. Belver, Effect of Activating Agent on the Properties of TiO₂/Activated Carbon Heterostructures for Solar Photocatalytic Degradation of Acetaminophen, Vol. 12, Page 378. 12, *Materials* 2019 (2019) 378, <https://doi.org/10.3390/MA12030378>.
- [39] M. Peñas-Garzón, M.J. Sampaio, Y.L. Wang, J. Bedia, J.J. Rodríguez, C. Belver, C. G. Silva, J.L. Faria, Solar photocatalytic degradation of parabens using UiO-66-NH₂, *Sep. Purif. Technol.* 286 (2022), 120467, <https://doi.org/10.1016/J.SEPPUR.2022.120467>.
- [40] R.R. Solís, M. Peñas-Garzón, C. Belver, J.J. Rodríguez, J. Bedia, Highly stable UiO-66-NH₂ by the microwave-assisted synthesis for solar photocatalytic water treatment, *J. Environ. Chem. Eng.* 10 (2022), 107122, <https://doi.org/10.1016/J.JECE.2021.107122>.
- [41] C. Baumanis, D.W. Bahnemann, TiO₂ Thin Film Electrodes: Correlation between Photocatalytic Activity and Electrochemical Properties, *J. Phys. Chem. C* 112 (2008) 19097–19101, <https://doi.org/10.1021/JP807655A>.
- [42] T. Giannakopoulou, I. Papailias, N. Todorova, N. Boukos, Y. Liu, J. Yu, C. Trapalis, Tailoring the energy band gap and edges' potentials of g-C₃N₄/TiO₂ composite photocatalysts for NO_x removal, *Chem. Eng. J.* 310 (2017) 571–580, <https://doi.org/10.1016/J.CEJ.2015.12.102>.
- [43] G.P. Anipsitakis, D.D. Dionysiou, Degradation of organic contaminants in water with sulfate radicals generated by the conjunction of peroxymonosulfate with cobalt, *Environ. Sci. Technol.* 37 (2003) 4790–4797, <https://doi.org/10.1021/es0263792>.
- [44] V. Muelas-Ramos, C. Belver, J.J. Rodríguez, J. Bedia, Synthesis of noble metal-decorated NH₂-MIL-125 titanium MOF for the photocatalytic degradation of acetaminophen under solar irradiation, *Sep. Purif. Technol.* 272 (2021), 118896, <https://doi.org/10.1016/J.SEPPUR.2021.118896>.
- [45] S. Chen, D. Huang, L. Du, L. Lei, Y. Chen, G. Wang, Z. Wang, W. Zhou, J. Tao, R. Li, C. Zhou, Peroxymonosulfate activation by surface-modified bismuth vanadate for ciprofloxacin abatement under visible light: Insights into the generation of singlet oxygen, *Chem. Eng. J.* 444 (2022), 136373, <https://doi.org/10.1016/J.CEJ.2022.136373>.
- [46] A.R. Patel, G. Patel, G. Maity, S.P. Patel, S. Bhattacharya, A. Putta, S. Banerjee, Direct Oxidative Azo Coupling of Anilines Using a Self-Assembled Flower-like CuCo₂O₄ Material as a Catalyst under Aerobic Conditions, *ACS Omega* 5 (2020) 30416–30424, https://doi.org/10.1021/ACSOMEGA.0C03562/SUPPL_FILE/AO0C03562_SI_001.PDF.
- [47] K.A. Cychoz, M. Thommes, Progress in the Physisorption Characterization of Nanoporous Gas Storage Materials, *Engineering* 4 (2018) 559–566, <https://doi.org/10.1016/J.ENG.2018.06.001>.
- [48] Y. Wang, J. Zhao, X. Xiong, S. Liu, Y. Xu, Role of Ni²⁺ ions in TiO₂ and Pt/TiO₂ photocatalysis for phenol degradation in aqueous suspensions, *Appl. Catal. B: Environ.* 258 (2019), 117903, <https://doi.org/10.1016/J.APCATB.2019.117903>.
- [49] M. Nowak, B. Kauch, P. Szperlich, Determination of energy band gap of nanocrystalline SbSI using diffuse reflectance spectroscopy, *Rev. Sci. Instrum.* 80 (2009), 046107, <https://doi.org/10.1063/1.3103603>.
- [50] G.P. Anipsitakis, D.D. Dionysiou, Transition metal/UV-based advanced oxidation technologies for water decontamination, *Appl. Catal. B: Environ.* 54 (2004) 155–163, <https://doi.org/10.1016/J.APCATB.2004.05.025>.
- [51] J. Lee, U. von Gunten, J.H. Kim, Persulfate-Based Advanced Oxidation: Critical Assessment of Opportunities and Roadblocks, *Environ. Sci. Technol.* 54 (2020) 3064–3081, https://doi.org/10.1021/ACS.EST.9B07082/ASSET/IMAGES/ACS.EST.9B07082.SOCIAL.JPEG_V03.
- [52] I. Berruti, I. Oller, M.I. Polo-López, Direct oxidation of peroxymonosulfate under natural solar radiation: Accelerating the simultaneous removal of organic contaminants and pathogens from water, *Chemosphere* 279 (2021), 130555, <https://doi.org/10.1016/J.CHEMOSPHERE.2021.130555>.
- [53] L. Yang, L. Xu, X. Bai, P. Jin, Enhanced visible-light activation of persulfate by Ti³⁺-self-doped TiO₂/graphene nanocomposite for the rapid and efficient degradation of micropollutants in water, *J. Hazard. Mater.* 365 (2019) 107–117, <https://doi.org/10.1016/J.JHAZMAT.2018.10.090>.
- [54] J. Yan, J. Li, J. Peng, H. Zhang, Y. Zhang, B. Lai, Efficient degradation of sulfamethoxazole by the CuO@Al₂O₃ (EPC) coupled PMS system: Optimization, degradation pathways and toxicity evaluation, *Chem. Eng. J.* 359 (2019) 1097–1110, <https://doi.org/10.1016/J.CEJ.2018.11.074>.
- [55] L. Zhu, Z. Shi, L. Deng, Enhanced heterogeneous degradation of sulfamethoxazole via peroxymonosulfate activation with novel magnetic MnFe₂O₄/GCNS nanocomposite, *Colloids Surf. A: Physicochem. Eng. Asp.* 621 (2021), 126531, <https://doi.org/10.1016/J.COLSURFA.2021.126531>.
- [56] S. Wang, W. Xu, J. Wu, Q. Gong, P. Xie, Improved sulfamethoxazole degradation by the addition of MoS₂ into the Fe²⁺/peroxymonosulfate process, *Sep. Purif. Technol.* 235 (2020), 116170, <https://doi.org/10.1016/J.SEPPUR.2019.116170>.
- [57] H. Diarmand-Khalilabad, A. Habibi-Yangjeh, D. Seifzadeh, S. Asadzadeh-Khaneghah, E. Vesali-Kermani, g-C₃N₄ nanosheets decorated with carbon dots and CdS nanoparticles: Novel nanocomposites with excellent nitrogen photofixation ability under simulated solar irradiation, *Ceram. Int.* 45 (2019) 2542–2555, <https://doi.org/10.1016/J.CERAMINT.2018.10.185>.
- [58] R.R. Solís, A. Gómez-Avilés, C. Belver, J.J. Rodríguez, J. Bedia, Microwave-assisted synthesis of NH₂-MIL-125(Ti) for the solar photocatalytic degradation of aqueous emerging pollutants in batch and continuous tests, *J. Environ. Chem. Eng.* 9 (2021), 106230, <https://doi.org/10.1016/J.JECE.2021.106230>.
- [59] A. Tolosana-Moranchel, J.A. Casas, A. Bahamonde, L. Pascual, L.I. Granone, J. Schneider, R. Dillert, D.W. Bahnemann, Nature and photoreactivity of TiO₂-rGO nanocomposites in aqueous suspensions under UV-A irradiation, *Appl. Catal. B: Environ.* 241 (2019) 375–384, <https://doi.org/10.1016/J.APCATB.2018.09.070>.
- [60] J. Wang, S. Wang, Activation of persulfate (PS) and peroxymonosulfate (PMS) and application for the degradation of emerging contaminants, *Chem. Eng. J.* 334 (2018) 1502–1517, <https://doi.org/10.1016/J.CEJ.2017.11.059>.
- [61] M. Peñas-Garzón, A. Gómez-Avilés, C. Belver, J.J. Rodríguez, J. Bedia, Degradation pathways of emerging contaminants using TiO₂-activated carbon heterostructures in aqueous solution under simulated solar light, *Chem. Eng. J.* 392 (2020), 124867, <https://doi.org/10.1016/J.CEJ.2020.124867>.
- [62] Y. Li, W. Zhu, Q. Guo, X. Wang, L. Zhang, X. Gao, Y. Luo, Highly efficient degradation of sulfamethoxazole (SMX) by activating peroxymonosulfate (PMS) with CoFe₂O₄ in a wide pH range, *Sep. Purif. Technol.* 276 (2021), 119403, <https://doi.org/10.1016/J.SEPPUR.2021.119403>.
- [63] L. Zhao, Z. Sun, J. Ma, H. Liu, Influencing mechanism of bicarbonate on the catalytic ozonation of nitrobenzene in aqueous solution by ceramic honeycomb supported manganese, *J. Mol. Catal. A: Chem.* 322 (2010) 26–32, <https://doi.org/10.1016/J.MOLCATA.2010.02.007>.
- [64] R. Guo, Y. Wang, J. Li, X. Cheng, D.D. Dionysiou, Sulfamethoxazole degradation by visible light assisted peroxymonosulfate process based on nanohybrid manganese dioxide incorporating ferric oxide, *Appl. Catal. B: Environ.* 278 (2020), 119297, <https://doi.org/10.1016/J.APCATB.2020.119297>.
- [65] Y. Zhou, J. Jiang, Y. Gao, J. Ma, S.Y. Pang, J. Li, X.T. Lu, L.P. Yuan, Activation of Peroxymonosulfate by Benzoquinone: A Novel Nonradical Oxidation Process, *Environ. Sci. Technol.* 49 (2015) 12941–12950, https://doi.org/10.1021/ACS.EST.5B03595/SUPPL_FILE/ESSB03595_SI_001.PDF.
- [66] S. Liu, Z. Zhang, F. Huang, Y. Liu, L. Feng, J. Jiang, L. Zhang, F. Qi, C. Liu, Carbonized polyaniline activated peroxymonosulfate (PMS) for phenol degradation: Role of PMS adsorption and singlet oxygen generation, *Appl. Catal. B: Environ.* 286 (2021), 119921, <https://doi.org/10.1016/J.APCATB.2021.119921>.
- [67] V.-H. Nguyen, S. Ali Delbari, M. Mousavi, A. Sabahi Namini, J.B. Ghasemi, Q. van Le, M. Shahedi Asl, M. Mohammadi, M. Shokouhimehr, g-C₃N₄-nanosheet/ZnCr₂O₄ S-scheme heterojunction photocatalyst with enhanced visible-light photocatalytic activity for degradation of phenol and tetracycline, *Sep. Purif. Technol.* (2021), 118511, <https://doi.org/10.1016/J.SEPPUR.2021.118511>.
- [68] M. Xu, T. Ye, F. Dai, J. Yang, J. Shen, Q. He, W. Chen, N. Liang, J. Zai, X. Qian, Rationally designed n-n heterojunction with highly efficient solar hydrogen evolution, *ChemSusChem* 8 (2015) 1218–1225, <https://doi.org/10.1002/CSSC.201403334>.
- [69] C. Luo, J. Ma, J. Jiang, Y. Liu, Y. Song, Y. Yang, Y. Guan, D. Wu, Simulation and comparative study on the oxidation kinetics of atrazine by UV/H₂O₂, UV/HSO₅[−] and UV/S₂O₈^{2−}, *Water Res.* 80 (2015) 99–108, <https://doi.org/10.1016/J.WATRES.2015.05.019>.
- [70] S. Wacławek, H. v Lütze, K. Grübel, V.V.T. Padil, M. Černík, D.D. Dionysiou, Chemistry of persulfates in water and wastewater treatment: A review, *Chem. Eng. J.* 330 (2017) 44–62, <https://doi.org/10.1016/J.CEJ.2017.07.132>.
- [71] J. Lee, U. von Gunten, J.H. Kim, Persulfate-Based Advanced Oxidation: Critical Assessment of Opportunities and Roadblocks, *Environ. Sci. Technol.* 54 (2020) 3064–3081, https://doi.org/10.1021/ACS.EST.9B07082/ASSET/IMAGES/ACS.EST.9B07082.SOCIAL.JPEG_V03.